Exchange-enhanced Ultrastrong Magnon-Magnon Coupling in a Compensated Ferrimagnet

Lukas Liensberger,[1,2,*] Akashdeep Kamra,[3,†] Hannes Maier-Flaig,[1,2]
Stephan Geprägs,[1] Andreas Erb,[1] Sebastian T. B. Goennenwein,[4]
Rudolf Gross,[1,2,5,6] Wolfgang Belzig,[7] Hans Huebl,[1,2,5,6] and Mathias Weiler[1,2,‡]

[1] *Walther-Meißner-Institut, Bayerische Akademie der Wissenschaften, 85748 Garching, Germany*

[2] *Physik-Department, Technische Universität München, 85748 Garching, Germany*

[3] *Center for Quantum Spintronics, Department of Physics, Norwegian University of Science and Technology, 7491 Trondheim, Norway*

[4] *Institut für Festkörper- und Materialphysik, Technische Universität Dresden, 01062 Dresden, Germany*

[5] *Nanosystems Initiative Munich, 80799 Munich, Germany*

[6] *Munich Center for Quantum Science and Technology (MCQST), 80799 Munich, Germany*

[7] *Department of Physics, University of Konstanz, 78457 Konstanz, Germany*

(Dated: March 12, 2019)

Abstract

The ultrastrong coupling of (quasi-)particles has gained considerable attention due to its application potential and richness of the underlying physics. Coupling phenomena arising due to electromagnetic interactions are well explored. In magnetically ordered systems, the quantum-mechanical exchange-interaction should furthermore enable a fundamentally different coupling mechanism.

Here, we report the observation of ultrastrong intralayer exchange-enhanced magnon-magnon coupling in a compensated ferrimagnet. We experimentally study the spin dynamics in a gadolinium iron garnet single crystal using broadband ferromagnetic resonance. Close to the ferrimagnetic compensation temperature, we observe ultrastrong coupling of clockwise and anticlockwise magnon modes. The magnon-magnon coupling strength reaches more than 30% of the mode frequency and can be tuned by varying the direction of the external magnetic field. We theoretically explain the observed phenomenon in terms of an exchange-enhanced mode-coupling mediated by a weak cubic anisotropy.

The strong and ultrastrong interaction of light and matter is foundational for circuit quantum electrodynamics [1] and enables efficient manipulation and control of quantum systems [2, 3]. The realizations of strong spin-photon [4–6] and magnon-photon [7–12] coupling have established magnetic systems as viable platforms for frequency up-conversion [13, 14] and quantum state storage [15]. In all these cases, electromagnetic interactions, such as magnetic and electric dipolar interactions and magneto-optic effects, are fundamentally responsible for the coupling. These interactions are typically weak compared to the energy scales of the involved excitations themselves. In magnetically ordered systems, the energy scale relevant for the magnon-magnon interaction is the quantum mechanical exchange interaction. While it has been recently shown [16–18] that the weak interlayer exchange coupling between two magnetic materials can invoke magnon-magnon coupling, the much stronger intrinsic intralayer exchange has not yet been leveraged for coupling phenomena. Here, we report the experimental observation of ultrastrong intralayer exchange-enhanced magnon-magnon coupling in a compensated ferrimagnet with a magnon-magnon coupling rate reaching up to 37% of the characteristic magnon frequency. We furthermore demonstrate that the coupling rate can be continuously tuned from the ultrastrong to the weak regime.

The dipolar nature of the coupling between spins or magnons to photons in microwave cavities has two important consequences. First, the magnetic dipolar coupling is weak, limiting the single spin-photon coupling rates to the sub-kHz-regime [19]. Second, the effective coupling rate g_{eff} of a system of spins (magnons) scales with their number N as $g_{\mathrm{eff}} \propto \sqrt{N}$ [20]. Thus, increasing g_{eff} hinges on tuning the cavity filling factor [8] or the spin density (saturation magnetization) [7, 21] in a given volume. Therefore, strong magnon-photon or cavity-mediated magnon-magnon coupling [22, 23] requires large filling factors or photon wavelength-sized, i.e., macroscopic dimensions.

Here, we go beyond dipolar coupling mechanisms, and explore exchange-enhanced magnon-magnon coupling in a compensated, effectively two-sublattice ferrimagnet in the collinear state. This system can be viewed as a "quasi-antiferromagnet" due to nearly identical sublattice magnetizations $M_{\mathrm{A}} \gtrsim M_{\mathrm{B}}$. In Fig. 1, we sketch the dynamics of the two coupled spin sublattices. The classical Landau-Lifshitz description of the magnetization dynamics for the uniform modes predicts clockwise (cw) and counterclockwise (ccw) precessing modes [25] as well as linearly oscillating solutions, which we denote as spin-down, spin-up

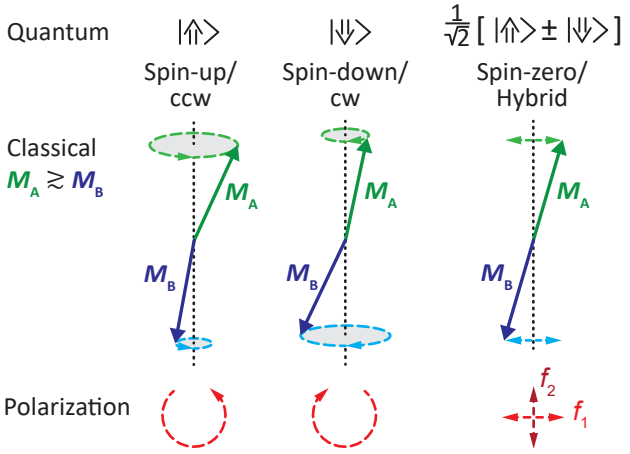

FIG. 1. **Classical and quantum representation of the magnetization dynamics of a two-sublattice spin system in a compensated ferrimagnet.** The classical magnetization dynamics of a compensated ferrimagnet close to its compensation temperature are similar to that of an antiferromagnet since the sublattice magnetizations are almost identical (we choose $M_{\mathrm{A}} \gtrsim M_{\mathrm{B}}$). In the quantum picture, the classical modes with counter-clockwise (ccw) and clockwise-precession (cw) are identified as spin-up and spin-down modes. The hybridized modes with linear polarization corresponds to spin-zero magnons [24]. The angles between the two sublattice magnetizations have been exaggerated for clarity.

and spin-zero excitations in a quantum picture. For a finite coupling between the spin-up and spin-down modes and the formation of a spin-zero hybridized state, spin-nonconserving interactions are required [24]. This mode mixing is associated with a breaking of rotational symmetry and leads to the lifting of the frequency degeneracy of orthogonal modes. Such a coupling can be induced by dipolar interactions [24], but is typically very weak. In this work, we show that a very weak magnetic anisotropy that locally fulfills the required axial symmetry breaking can have a strong effect via exchange-enhancement. This allows to push magnon-magnon coupling into the ultastrong coupling regime. Fundamentally, this coupling mechanism is independent of the magnetic volume (as long as it is larger than the sub-nm exchange length cubed λ_{ex}^3) due to the short-range nature of the exchange interaction.

In our corresponding experiments, we study the magnetization dynamics of a (111)-oriented single crystal $Gd_3Fe_5O_{12}$ (gadolinium iron garnet, GdIG) disk by broadband magnetic resonance (BMR) [26]. A schematic depiction of the setup is shown in Fig. 2(a), along

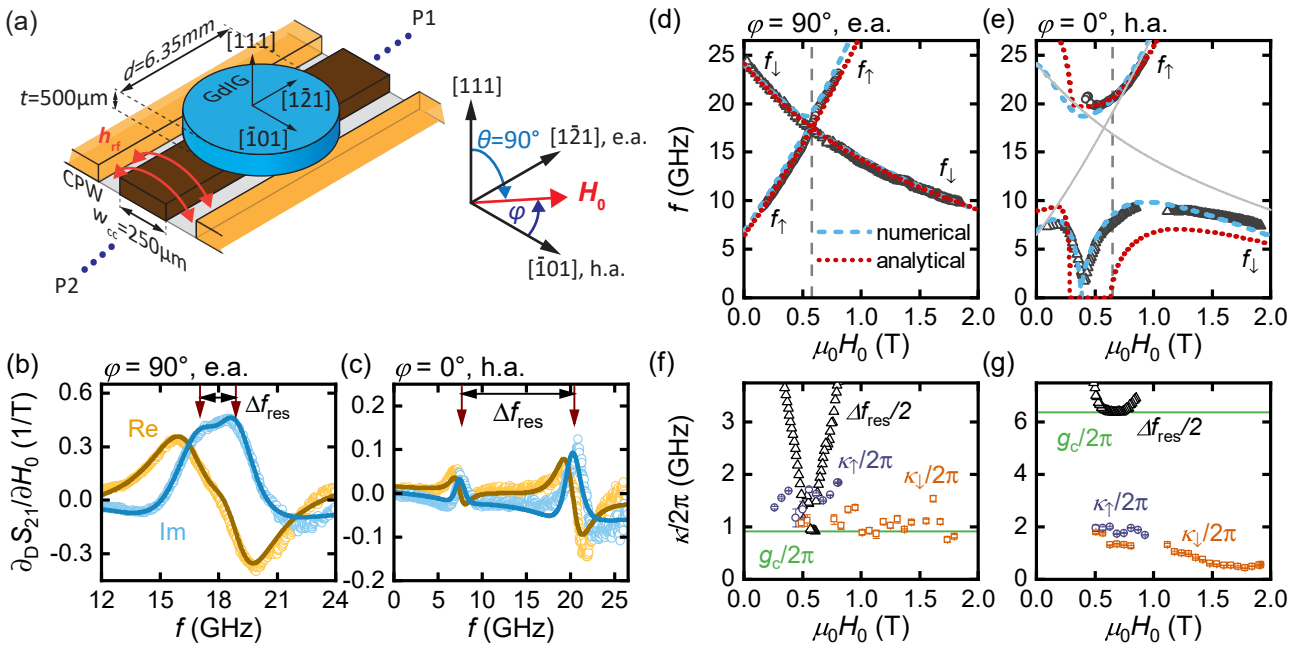

FIG. 2. **Broadband ferromagnetic resonance spectroscopy of ultrastrong magnon-magnon coupling.** (a) Schematic broadband ferromagnetic resonance (BMR) setup, with the GdIG disk on the coplanar waveguide (CPW). The angle φ defines the in-plane direction of the magnetic field $\boldsymbol{H}_0$ as shown in the coordinate system on the right. (b),(c) BMR spectra obtained for fixed magnetic field strengths applied along the (b) magnetically easy axis (e.a.) in the (111)-plane at $\varphi = 90°$ ($\mu_0 H_0 = 0.58\,\mathrm{T}$) and along the (c) magnetically hard axis (h.a.) $\varphi = 0°$ ($\mu_0 H_0 = 0.65\,\mathrm{T}$) recorded at $T = 282\,\mathrm{K}$ ($T_{\mathrm{comp}} = 288\,\mathrm{K}$). The solid lines are fits to Eq. (5). The resonance frequencies are indicated by the red arrows and their difference is denoted as Δf_{res}. (d),(e) Mode frequencies vs. applied magnetic field strength measured at $T = 282\,\mathrm{K}$ where $M_{\mathrm{Gd}} \gtrsim M_{\mathrm{Fe}}$. Open circles and triangles denote measured resonance frequencies. The red dotted curves depict results of the analytical model and the blue dashed lines are obtained by numerical simulation. Along the easy axis $\varphi = 90°$ (d), weak coupling is observed, whereas along the hard axis $\varphi = 0°$ (e), we find ultrastrong coupling (see text). The solid gray lines indicate the uncoupled case taken from the analytical solution of panel (d). (f),(g) Linewidth $\kappa/2\pi$ of the spin-up $\kappa_\uparrow$ and $\kappa_\downarrow$ modes and resonance frequency splitting $\Delta f_{\mathrm{res}}/2$ as a function of H_0. The coupling strength $g_{\mathrm{c}}/2\pi$ is given by the minimum of $\Delta f_{\mathrm{res}}/2$.

with a definition of the employed coordinate system. We use a vector network analyzer to record the complex transmission S_{21} as a function of the microwave frequency f and the external magnetic field $\boldsymbol{H}_0$ applied in the (111)-plane. Our experiments are performed at $T = 282\,\mathrm{K}$, slightly below the ferrimagnetic compensation point $T_{\mathrm{comp}} = 288\,\mathrm{K}$, as determined by SQUID-magnetometry (see Supplementary Information). At this temperature, the resonance frequencies of the spin-up and spin-down modes are in the microwave frequency range.

In Fig. 2(b), we show the normalized background-corrected field-derivative of S_{21} [27] recorded at fixed magnetic field magnitude $\mu_0 H_0 = 0.58\,\mathrm{T}$ applied at $\varphi = 90°$. As discussed later, this situation corresponds to $\boldsymbol{H}_0$ applied along an easy axis (e.a.) of the second-order cubic anisotropy. By fitting the data to Eq. (5), we extract the resonance frequencies f_1 and f_2 of the two observed resonances, their difference Δf_{res} and their linewidths κ_1 and κ_2. In Fig. 2(c) we show corresponding data and fits for $\varphi = 0°$ and $\mu_0 H_0 = 0.65\,\mathrm{T}$, where $\boldsymbol{H}_0$ was applied along a hard axis (h.a.) of the second order cubic anisotropy. Again, two resonances are observed. In contrast to the data in Fig. 2(b), the resonances are now clearly separated.

We repeat these experiments for a range of magnetic field magnitudes H_0 applied along the easy and hard axis. The obtained resonance frequencies are shown as symbols in Figs. 2(d) and (e). In the easy axis case shown in Fig. 2(d) we clearly observe two resonance modes. The first one follows $\partial f_{\mathrm{res}}/\partial H_0 > 0$ and is the spin-up mode $f_\uparrow$ and the second resonance with $\partial f_{\mathrm{res}}/\partial H_0 < 0$ is attributed to the spin-down mode $f_\downarrow$. The vertical dashed line corresponds to $\mu_0 H_0 = 0.58\,\mathrm{T}$ where Δf_{res} is minimized and the data shown in Fig. 2(b) is obtained. The resonance frequencies are in excellent agreement with those obtained from numerical (see Methods) and analytical (see below) solutions to the Landau-Lifshitz equation.

When applying $\boldsymbol{H}_0$ along the hard axis, we obtain the resonance frequencies shown in Fig. 2(e). Here, we observe a more complex evolution of the resonance frequencies for two reasons. First, for $\mu_0 H_0 \lessapprox 0.4\,\mathrm{T}$, the net magnetization is titled away from $\boldsymbol{H}_0$. Second, and crucially, the avoided crossing between the spin-up and spin-down modes is visible. The dashed vertical line indicates the value of H_0 of minimal Δf_{res} (c.f. Fig. 2(c)).

To elucidate the coupling further, we compare the linewidths of the respective modes to their mutual coupling strength g_{c}. To this end, we plot the frequency splitting of the two resonances Δf_{res} and the half-width-at-half-maximum (HWHM) linewidths of the spin-up mode $\kappa_\uparrow$ and the spin-down mode $\kappa_\downarrow$ as a function of the magnetic field H_0 in Figs. 2(f)

and (g) for the easy and hard axis case respectively. From the frequency splitting Δf_{res} we extract the coupling strength as $g_{\mathrm{c}}/2\pi = \min|\Delta f_{\mathrm{res}}/2|$. We find $g_{\mathrm{c}}/2\pi = 0.92\,\mathrm{GHz}$ for the easy axis case and $g_{\mathrm{c}}/2\pi = 6.38\,\mathrm{GHz}$ for the hard axis configuration. In the easy axis case, the extracted linewidths $\kappa_{\uparrow}$ and $\kappa_{\downarrow}$ for the two resonance modes are comparable or slightly larger than the coupling strength $g_{\mathrm{c}} \lesssim \kappa_{\uparrow}, \kappa_{\downarrow}$ (c.f. Fig. 2(f)). Thus, the system is in the weak to intermediate coupling regime. For the hard axis case, a pronounced anti-crossing between the two modes is observed in Fig. 2(e). In this case, the linewidths κ are at least three times smaller than the coupling strength g_{c}. Hence the condition for strong coupling $g_{\mathrm{c}} > \kappa_{\uparrow}, \kappa_{\downarrow}$ is clearly satisfied. Furthermore, the extracted coupling rate of $g_{\mathrm{c}}/2\pi = 6.38\,\mathrm{GHz}$ is comparable to the intrinsic excitation frequency $f_{\mathrm{r}} = (f_1 + f_2)/2 = 17.2\,\mathrm{GHz}$. The normalized coupling rate $\eta = g_{\mathrm{c}}/(2\pi f_{\mathrm{r}})$ [8, 28] evaluates to $\eta = 0.37$. Consequently, we observe magnon-magnon hybridization in the ultrastrong coupling regime [1]. Importantly, the measured g_{c} is the intrinsic coupling strength between spin-up and spin-down magnons. This coupling strength is independent of geometrical factors, in particular, sample volume or filling factor. This is in stark contrast to the magnon-photon coupling typically observed in spin cavitronics [8, 21].

To demonstrate that the coupling is continuously tunable between the extreme cases discussed so far, we rotated $\boldsymbol{H}_0$ with fixed magnitude in the (111)-plane at $T = 280\,\mathrm{K}$. The background corrected transmission parameter (see Supplementary Information) as a function of the angle φ is shown in Fig. 3(a) and (b) for $\mu_0 H_0 = 0.5\,\mathrm{T}$ and $\mu_0 H_0 = 0.8\,\mathrm{T}$, respectively. These magnetic field magnitudes correspond to H_0 slightly below and above the hybridization point at $T = 280\,\mathrm{K}$ as visible from Fig. S2 (see Supplementary Information). For both H_0 values, we observe two resonances for each value of φ, where the lower resonance frequency depends strongly on φ and the upper resonance frequency is nearly independent of φ. Overall, these results strongly indicate a φ-dependent level repulsion that allows to continuously adjust the coupling strength.

To understand the dependence of the coupling strength on φ, we analyze the cubic anisotropy landscape of our GdIG disk by plotting its magnetic free energy density F (c.f. Eq. (7)) in Fig. 3(c). The equilibrium orientations of the net magnetization for the easy and hard axis cases are indicated by grey dots in Fig. 3(c). From these two orientations, the orange arrows point towards increasing F and the white arrows towards decreasing F.

For the easy axis case, orange and white arrows point in opposite directions, while they

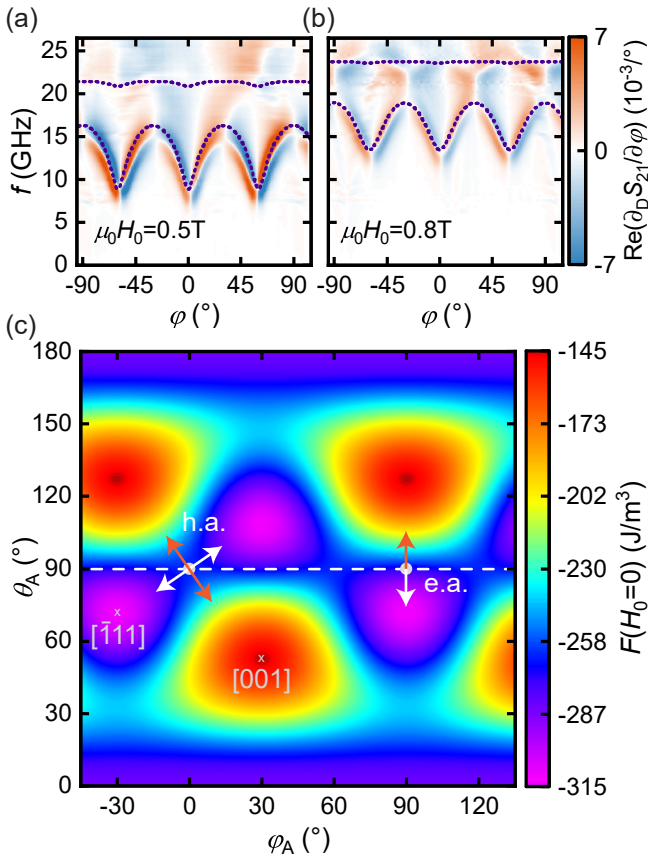

FIG. 3. **Tunable coupling strength and anisotropy landscape.** (a),(b) BMR-data obtained with fixed magnetic field magnitudes with (a) $\mu_0 H_0 = 0.5\,\mathrm{T}$ (below the hybridization point) and (b) $\mu_0 H_0 = 0.8\,\mathrm{T}$ (above the hybridization point) as a function of the $\boldsymbol{H}_0$-orientation φ in the (111)-disk plane at $T = 280\,\mathrm{K}$. The blue dashed lines are the results from the numerical simulation. (c) Colormap of the free energy density F for $H_0 = 0$. The angles φ_A and θ_A denote the orientation of M_A, defined analogously to φ and θ in Fig. 2(a). The dashed horizontal line at $\theta_\mathrm{A} = 90°$ corresponds to the (111)-disk plane. The orange and white arrows at the e.a. ($\varphi_\mathrm{A} = 90°$) and h.a. ($\varphi_\mathrm{A} = 0°$) point towards increasing and decreasing free energy density, respectively. The [001]-direction denotes a crystalline hard axis and [$\bar{1}$11] a crystalline easy axis.

are aligned orthogonally for the hard axis case. The 180° symmetry breaking of the easy axis case effectively cancels and restores axial symmetry [24], in agreement with the weak coupling found in Fig. 2(d). In contrast, we observe a 90° breaking of rotational symmetry for the hard axis case. This mediates formation of energetically distinct orthogonally polarized spin-zero magnons as discussed in the context of Fig. 1 and is in accordance with the ultrastrong

coupling observed in Fig. 2(e). Importantly, while the cubic anisotropies are very weak and would only result in a negligible magnon-magnon coupling on their own, their effect on the coupling is exchange-enhanced by the dynamically precessing magnetization as explained in the following.

We employ a two-sublattice model, which corresponds to the net Fe- and Gd-sublattice in GdIG, within the Landau-Lifshitz framework and macrospin approximation, treating anisotropies as uniaxial. This simple model captures the essential physics and provides physical insight based on an analytic solution. In practice, both of the distinct anisotropy contributions considered here are provided by the cubic crystalline anisotropy of the material. Parameterizing the intersublattice antiferromagnetic exchange by J (> 0) and uniaxial anisotropies by K (> 0) and K_a, the free energy density F_m is expressed in terms of the sublattice A and B magnetizations $\boldsymbol{M}_\mathrm{A,B}$, assumed spatially uniform, as

$$F_\mathrm{m} = -\mu_0 H_0(M_{\mathrm{A}z} + M_{\mathrm{B}z}) \mp K\left(M_{\mathrm{A}z}^2 + M_{\mathrm{B}z}^2\right) + K_\mathrm{a}\left(M_{\mathrm{A}x}^2 + M_{\mathrm{B}x}^2\right) + J\boldsymbol{M}_\mathrm{A}\cdot\boldsymbol{M}_\mathrm{B}, \qquad (1)$$

where the first term is the Zeeman contribution due to the applied field $H_0\hat{\boldsymbol{z}}$. We further assume an appropriate hierarchy of interactions $J \gg K \gg |K_\mathrm{a}|$, such that K_a terms do not influence the equilibrium configurations. The upper and lower signs in Eq. (1) above represent the cases of an applied field along easy and hard axes, respectively. The equilibrium configuration is obtained by minimizing the free energy density [Eq. (1)] with respect to the sublattice magnetization directions (see Supplementary Information). The dynamics are captured by the Landau-Lifshitz equations for the two sublattices:

$$\frac{\partial \boldsymbol{M}_\mathrm{A,B}}{\partial t} = -|\gamma_\mathrm{A,B}|\left[\boldsymbol{M}_\mathrm{A,B}\times\left(-\frac{\partial F_\mathrm{m}}{\partial \boldsymbol{M}_\mathrm{A,B}}\right)\right], \qquad (2)$$

where $\gamma_\mathrm{A,B}$ are the respective sublattice gyromagnetic ratios, assumed negative. It is convenient to employ a new primed coordinate system with equilibrium magnetizations collinear with $\hat{\boldsymbol{z}}'$. The ensuing dynamical equations are linearized about the equilibrium configuration which, on switching to Fourier space (i.e. $M_{\mathrm{A}x'} = m_{\mathrm{A}x'}e^{i\omega t}$ and so on), lead to the coupled equations describing the eigenmodes expressed succinctly as a 4×4 matrix equation:

$$\left(\tilde{P}_0 + \tilde{P}_\mathrm{a}\right)\tilde{m} = 0, \qquad (3)$$

where $\tilde{m}^\intercal = [m_{\mathrm{A}+}\ m_{\mathrm{B}+}\ m_{\mathrm{A}-}\ m_{\mathrm{B}-}]$ with $m_{\mathrm{A}\pm} \equiv m_{\mathrm{A}x'} \pm i m_{\mathrm{A}y'}$ and so on. The matrix $\tilde{P}_0$ is block diagonal in 2×2 sub-matrices and describes the uncoupled spin-up and spin-down

modes, distributed over both sublattices. The matrix $\tilde{P}_\mathrm{a}$ captures axial-symmetry-breaking anisotropy effects, and provides the spin-nonconserving, off-diagonal terms that couple the two modes and underlie the hybridization physics at play. The detailed expressions for the matrices are provided in the Supplementary Information.

For the experimentally applied fields along the easy-axis, the equilibrium configuration is given by $\boldsymbol{M}_\mathrm{A} = M_\mathrm{A0}\hat{\boldsymbol{z}}$ and $\boldsymbol{M}_\mathrm{B} = -M_\mathrm{B0}\hat{\boldsymbol{z}}$, with $M_\mathrm{A0,B0}$ the respective sublattice saturation magnetizations and $M_\mathrm{A0} \gtrsim M_\mathrm{B0}$. As a result, only the K_a anisotropy term breaks axial symmetry about the equilibrium magnetization direction (z-axis) and leads to off-diagonal terms in $\tilde{P}_\mathrm{a}$, which couples the two modes. For the case of a field applied along the hard axis with very small magnitude, the equilibrium orientation of $\boldsymbol{M}_\mathrm{A}$ is orthogonal to the hard axis. With increasing field strength, $\boldsymbol{M}_\mathrm{A}$ moves to align with the applied field. In the considered temperature and field range, $\boldsymbol{M}_\mathrm{B}$ always remains essentially anticollinear to $\boldsymbol{M}_\mathrm{A}$ [29]. The initial decrease of the resonance mode with lower frequency [Fig. 2(e)] is associated with this evolution of the equilibrium configuration. The frequency dip signifies alignment of equilibrium $\boldsymbol{M}_\mathrm{A}$ with the z-axis, which is maintained with further increase in the field strength. The coupling-mediated frequency splitting Δf_res, where uncoupled eigenmode frequencies would cross, is evaluated employing Eq. (3) as:

$$2\pi\Delta f_\mathrm{res} = \omega_\mathrm{c}\sqrt{\frac{16JM_0^2}{J\left(M_\mathrm{A0}-M_\mathrm{B0}\right)^2 + F_\mathrm{eq}}}, \tag{4}$$

where $\omega_\mathrm{c} \equiv |\gamma||K_\mathrm{a}|M_0$ is the bare coupling rate, considering $\gamma_\mathrm{A} \approx \gamma_\mathrm{B} \equiv \gamma$ and $M_\mathrm{A0} \approx M_\mathrm{B0} \equiv M_0$ near the compensation point. F_eq, given by $16KM_0^2$ for the easy-axis configuration, is an equivalent free energy density comparable to the anisotropy contribution, parametrized by K. The bare coupling rate is thus boosted up to a maximum value of $\sqrt{J/K}$ at the compensation point yielding to a greatly enhanced coupling. Hereby a small coupling of $\omega_\mathrm{c} = 2\pi \cdot 160\,\mathrm{MHz}$ originating from a weak cubic anisotropy present in GdIG is greatly enhanced as shown by the analytical model displayed in Fig. 2(e), quantitatively describing our experimental observations. The amplification of coupling from 160 MHz to several GHz is an exchange-enhancement effect [30–32]. This (exchange-) enhancement is an embodiment of antiferromagnetic quantum fluctuations predicted similarly to amplify magnon-mediated superconductivity [33].

Our findings demonstrate that previously typically neglected details of the magnetocrystalline anisotropy can lead to giant effects on spin-dynamics if they have the appropriate sym-

metry and are exchange-enhanced. The ultrastrong and size-independent magnon-magnon coupling reported here opens exciting perspectives for studying ultrastrong coupling effects in nanoscale devices and exploring quantum-mechanical coupling phenomena beyond classical electrodynamics. The reported effect also enables the tuning and tailoring of quasi-antiferromagnetic dynamics.

Note added: During the preparation of the manuscript, we became aware of a related study showing magnon-magnon coupling in the canted antiferromagnet $CrCl_3$ [34].

Acknowledgments. – We thank A. Habel, K. Helm-Knapp, and K. Danielewicz for technical support. We gratefully acknowledge the financial support of the Deutsche Forschungsgemeinschaft (DFG, German Research Foundation) via Germany's Excellence Strategy EXC-2111-390814868 (R.G. and H.H.) and the projects WE5386/4 and WE5386/5 (L.L. and M.W.). A.K. acknowledges financial support from the Research Council of Norway through its Centers of Excellence funding scheme, project 262633, "QuSpin". W.B. was supported by the DFG through SFB 767 and thanks the Center of Excellence QuSpin by the Research Council of Norway and Arne Brataas (NTNU Trondheim) for hospitality.

* Lukas.Liensberger@wmi.badw.de

† Akashdeep.Kamra@ntnu.no

‡ Mathias.Weiler@wmi.badw.de

[1] A. Frisk Kockum, A. Miranowicz, S. De Liberato, S. Savasta, and F. Nori, Ultrastrong coupling between light and matter, Nature Reviews Physics **1**, 19 (2019).

[2] X. Zhu, S. Saito, A. Kemp, K. Kakuyanagi, S.-i. Karimoto, H. Nakano, W. J. Munro, Y. Tokura, M. S. Everitt, K. Nemoto, M. Kasu, N. Mizuochi, and K. Semba, Coherent coupling of a superconducting flux qubit to an electron spin ensemble in diamond, Nature **478**, 221 (2011).

[3] J. J. Viennot, M. C. Dartiailh, A. Cottet, and T. Kontos, Coherent coupling of a single spin to microwave cavity photons, Science **349**, 408 (2015).

[4] D. I. Schuster, A. P. Sears, E. Ginossar, L. DiCarlo, L. Frunzio, J. J. L. Morton, H. Wu, G. A. D. Briggs, B. B. Buckley, D. D. Awschalom, and R. J. Schoelkopf, High-Cooperativity Coupling of Electron-Spin Ensembles to Superconducting Cavities, Physical Review Letters

105, 140501 (2010).

[5] Y. Kubo, F. R. Ong, P. Bertet, D. Vion, V. Jacques, D. Zheng, A. Dréau, J.-F. Roch, A. Auffeves, F. Jelezko, J. Wrachtrup, M. F. Barthe, P. Bergonzo, and D. Esteve, Strong Coupling of a Spin Ensemble to a Superconducting Resonator, Physical Review Letters **105**, 140502 (2010).

[6] N. Samkharadze, G. Zheng, N. Kalhor, D. Brousse, A. Sammak, U. C. Mendes, A. Blais, G. Scappucci, and L. M. K. Vandersypen, Strong spin-photon coupling in silicon, Science **359**, 1123 (2018).

[7] H. Huebl, C. W. Zollitsch, J. Lotze, F. Hocke, M. Greifenstein, A. Marx, R. Gross, and S. T. B. Goennenwein, High Cooperativity in Coupled Microwave Resonator Ferrimagnetic Insulator Hybrids, Physical Review Letters **111**, 127003 (2013).

[8] X. Zhang, C. L. Zou, L. Jiang, and H. X. Tang, Strongly coupled magnons and cavity microwave photons, Physical Review Letters **113**, 156401 (2014).

[9] L. Bai, M. Harder, Y. P. Chen, X. Fan, J. Q. Xiao, and C.-M. Hu, Spin Pumping in Electrodynamically Coupled Magnon-Photon Systems, Physical Review Letters **114**, 227201 (2015).

[10] T. Liu, X. Zhang, H. X. Tang, and M. E. Flatté, Optomagnonics in magnetic solids, Physical Review B **94**, 060405 (2016).

[11] S. Viola Kusminskiy, H. X. Tang, and F. Marquardt, Coupled spin-light dynamics in cavity optomagnonics, Physical Review A **94**, 033821 (2016).

[12] M. Harder and C.-M. Hu, Cavity Spintronics: An Early Review of Recent Progress in the Study of MagnonPhoton Level Repulsion, in *Solid State Physics 69*, edited by R. E. Camley and R. L. Stamps (Academic Press, Cambridge, 2018) pp. 47–121.

[13] R. Hisatomi, A. Osada, Y. Tabuchi, T. Ishikawa, A. Noguchi, R. Yamazaki, K. Usami, and Y. Nakamura, Bidirectional conversion between microwave and light via ferromagnetic magnons, Physical Review B **93**, 174427 (2016).

[14] S. Klingler, H. Maier-Flaig, R. Gross, C.-M. Hu, H. Huebl, S. T. B. Goennenwein, and M. Weiler, Combined Brillouin light scattering and microwave absorption study of magnon-photon coupling in a split-ring resonator/YIG film system, Applied Physics Letters **109**, 072402 (2016).

[15] Y. Tabuchi, S. Ishino, A. Noguchi, T. Ishikawa, R. Yamazaki, K. Usami, and Y. Nakamura, Coherent coupling between a ferromagnetic magnon and a superconducting qubit, Science

349, 405 (2015).

[16] S. Klingler, V. Amin, S. Geprägs, K. Ganzhorn, H. Maier-Flaig, M. Althammer, H. Huebl, R. Gross, R. D. McMichael, M. D. Stiles, S. T. Goennenwein, and M. Weiler, Spin-Torque Excitation of Perpendicular Standing Spin Waves in Coupled YIG/Co Heterostructures, Physical Review Letters **120**, 127201 (2018).

[17] J. Chen, C. Liu, T. Liu, Y. Xiao, K. Xia, G. E. W. Bauer, M. Wu, and H. Yu, Strong Interlayer Magnon-Magnon Coupling in Magnetic Metal-Insulator Hybrid Nanostructures, Physical Review Letters **120**, 217202 (2018).

[18] H. Qin, S. J. Hämäläinen, and S. van Dijken, Exchange-torque-induced excitation of perpendicular standing spin waves in nanometer-thick YIG films, Scientific Reports **8**, 5755 (2018).

[19] C. Eichler, A. J. Sigillito, S. A. Lyon, and J. R. Petta, Electron Spin Resonance at the Level of 10^4 Spins Using Low Impedance Superconducting Resonators, Physical Review Letters **118**, 037701 (2017).

[20] M. Tavis and F. W. Cummings, Exact Solution for an N-Molecule-Radiation-Field Hamiltonian, Physical Review **170**, 379 (1968).

[21] H. Maier-Flaig, M. Harder, S. Klingler, Z. Qiu, E. Saitoh, M. Weiler, S. Geprägs, R. Gross, S. T. B. Goennenwein, and H. Huebl, Tunable magnon-photon coupling in a compensating ferrimagnet - from weak to strong coupling, Applied Physics Letters **110**, 132401 (2017).

[22] B. Zare Rameshti and G. E. W. Bauer, Indirect coupling of magnons by cavity photons, Physical Review B **97**, 014419 (2018).

[23] Ø. Johansen and A. Brataas, Nonlocal Coupling between Antiferromagnets and Ferromagnets in Cavities, Physical Review Letters **121**, 087204 (2018).

[24] A. Kamra, U. Agrawal, and W. Belzig, Noninteger-spin magnonic excitations in untextured magnets, Physical Review B **96**, 020411 (2017).

[25] A. Gurevich and G. Melkov, *Magnetization Oscillations and Waves* (CRC Press, Taylor & Francis Group, 1996).

[26] S. S. Kalarickal, P. Krivosik, M. Wu, C. E. Patton, M. L. Schneider, P. Kabos, T. J. Silva, and J. P. Nibarger, Ferromagnetic resonance linewidth in metallic thin films: Comparison of measurement methods, Journal of Applied Physics **99**, 093909 (2006).

[27] H. Maier-Flaig, S. T. B. Goennenwein, R. Ohshima, M. Shiraishi, R. Gross, H. Huebl, and M. Weiler, Note: Derivative divide, a method for the analysis of broadband ferromagnetic

resonance in the frequency domain, Review of Scientific Instruments **89**, 076101 (2018).

[28] T. Niemczyk, F. Deppe, H. Huebl, E. P. Menzel, F. Hocke, M. J. Schwarz, J. J. Garcia-Ripoll, D. Zueco, T. Hümmer, E. Solano, A. Marx, and R. Gross, Beyond the Jaynes-Cummings model: circuit QED in the ultrastrong coupling regime, Nature Physics **6**, 772 (2010).

[29] K. Ganzhorn, J. Barker, R. Schlitz, B. A. Piot, K. Ollefs, F. Guillou, F. Wilhelm, A. Rogalev, M. Opel, M. Althammer, S. Geprägs, H. Huebl, R. Gross, G. E. W. Bauer, and S. T. B. Goennenwein, Spin Hall magnetoresistance in a canted ferrimagnet, Physical Review B **94**, 094401 (2016).

[30] G. P. Rodrigue, H. Meyer, and R. V. Jones, Resonance Measurements in Magnetic Garnets, Journal of Applied Physics **31**, S376 (1960).

[31] F. Keffer and C. Kittel, Theory of Antiferromagnetic Resonance, Physical Review **85**, 329 (1952).

[32] A. Kamra, R. E. Troncoso, W. Belzig, and A. Brataas, Gilbert damping phenomenology for two-sublattice magnets, Physical Review B **98**, 184402 (2018).

[33] E. Erlandsen, A. Kamra, A. Brataas, and A. Sudbø, Superconductivity enhancement on a topological insulator surface by antiferromagnetic squeezed magnons, arXiv:1903.01470 (2019).

[34] D. MacNeill, J. T. Hou, D. R. Klein, P. Zhang, P. Jarillo-Herrero, and L. Liu, Gigahertz frequency antiferromagnetic resonance and strong magnon-magnon coupling in the layered crystal CrCl3, arXiv:1902.05669 (2019).

[35] D. Polder, VIII. On the theory of ferromagnetic resonance, The London, Edinburgh, and Dublin Philosophical Magazine and Journal of Science **40**, 99 (1949).

[36] G. F. Dionne, *Magnetic Oxides* (Springer US, Boston, MA, 2009).

[37] S. Koohpayeh, Single crystal growth by the traveling solvent technique: A review, Progress in Crystal Growth and Characterization of Materials **62**, 22 (2016).

[38] L. Dreher, M. Weiler, M. Pernpeintner, H. Huebl, R. Gross, M. S. Brandt, and S. T. B. Goennenwein, Surface acoustic wave driven ferromagnetic resonance in nickel thin films: Theory and experiment, Physical Review B **86**, 134415 (2012).

[39] J. A. Osborn, Demagnetizing Factors of the General Ellipsoid, Physical Review **67**, 351 (1945).

METHODS

Fitting routine

In order to quantitatively extract the resonance frequencies $\omega_{\mathrm{res}} = 2\pi f_{\mathrm{res}}$ and the half-width-at-half-maximum linewidths κ, the real and imaginary part of $\partial_{\mathrm{D}} S_{21}/\partial H_0$ are fitted at fixed magnetic field to [16, 27]

$$\partial_{\mathrm{D}} S_{21}/\partial H_0|_{H_0} = -A' \frac{\chi(\omega, H_0 + \Delta H) - \chi(\omega, H_0 - \Delta H)}{(A'\chi(\omega, H_0) + 1) \cdot \Delta H} + C, \tag{5}$$

where A' is a complex amplitude, χ is a diagonal component of the Polder susceptibility, which describes the response of the dynamical component of the magnetization to an external oscillating magnetic field [35], ΔH is the field step size of $10\,\mathrm{mT}/\mu_0$ and $C = C_0 + C_1 H_0$ is a complex linear offset. For the fitting, we use for the susceptibility normalized to the saturation magnetization [27]

$$\chi(\omega, H_0) = \frac{|\gamma'|\mu_0 H_0 - i2\kappa}{\omega_{\mathrm{res}}^2 - \omega^2 - i\omega\, 2\kappa}. \tag{6}$$

with $|\gamma'|$ the gyromagnetic ratio.

Material

Gadolinium iron garnet ($Gd_3Fe_5O_{12}$, GdIG) is a compensated ferrimagnet consisting of three magnetic sublattices. The two nearly temperature-independent iron-sublattice magnetizations couple strongly antiferromagnetically to each other. They can be treated as one effective iron-sublattice. GdIG features a strongly temperature-dependent gadolinium-sublattice magnetization which is antiferromagnetically coupled to the iron-sublattice [36] in the considered temperature and magnetic field range, resulting in an effective two-sublattice system. Due to the temperature-dependence of the Gd-sublattice a compensation of the sublattice magnetizations occurs, where the net remanent magnetization vanishes at the so-called compensation temperature T_{comp} which we determined with SQUID magnetometry measurements to $T_{\mathrm{comp}} = 288\,\mathrm{K}$. From temperature-dependent SQUID magnetometry measurements, we obtain the magnitude of both sublattice magnetizations as detailed in the Supplementary Information.

The single crystal GdIG disk was grown using traveling solvent floating zone method [37] and cut to a (111)-oriented disk with diameter $d = 6.35\,\mathrm{mm}$ and thickness $t = 500\,\mu\mathrm{m}$.

Numerical model

Our numerical analysis follows the approach by Dreher *et al.* [38]. We start with the free energy density

$$\begin{aligned} F =& J\,\boldsymbol{M}_{\mathrm{A}}\cdot\boldsymbol{M}_{\mathrm{B}} - \mu_0\boldsymbol{H}_0\cdot(\boldsymbol{M}_{\mathrm{A}}+\boldsymbol{M}_{\mathrm{B}}) + \frac{\mu_0}{2}(\boldsymbol{M}_{\mathrm{A}}+\boldsymbol{M}_{\mathrm{B}})\overleftrightarrow{N}(\boldsymbol{M}_{\mathrm{A}}+\boldsymbol{M}_{\mathrm{B}}) \\ &+ K_{c1}(\alpha_{\mathrm{A}}^2\beta_{\mathrm{A}}^2+\alpha_{\mathrm{A}}^2\delta_{\mathrm{A}}^2+\beta_{\mathrm{A}}^2\delta_{\mathrm{A}}^2+\alpha_{\mathrm{B}}^2\beta_{\mathrm{B}}^2+\alpha_{\mathrm{B}}^2\delta_{\mathrm{B}}^2+\beta_{\mathrm{B}}^2\delta_{\mathrm{B}}^2) + K_{c2}(\alpha_{\mathrm{A}}^2\beta_{\mathrm{A}}^2\delta_{\mathrm{A}}^2+\alpha_{\mathrm{B}}^2\beta_{\mathrm{B}}^2\delta_{\mathrm{B}}^2), \end{aligned} \tag{7}$$

where $\alpha_{\mathrm{A,B}}$, $\beta_{\mathrm{A,B}}$ and $\delta_{\mathrm{A,B}}$ are the direction cosines of the magnetizations $\boldsymbol{M}_{\mathrm{A,B}}$ with respect to the cubic (100)-axes, J is the intersublattice antiferromagnetic exchange constant, $\overleftrightarrow{N}$ is the demagnetization tensor for the disk-shaped sample [39], and K_{c1} and K_{c2} are the 1st and 2nd order cubic anisotropy constants. The subscripts A and B refer to the Gd- and Fe-sublattices, respectively. The lengths of the $\boldsymbol{M}_{\mathrm{A,B}}$ vectors are the saturation magnetizations $M_{\mathrm{B}}^{\mathrm{s}} = M_{\mathrm{B0}}$ and $M_{\mathrm{A}}^{\mathrm{s}} = M_{\mathrm{A0}} + \chi_{\mathrm{a}}H_0$, where we account for a field-dependent Gd-magnetization. For the plot of F in Fig. 3(c), we set $M_{\mathrm{B0}} = 0$ and $M_{\mathrm{A0}} = 10\,\mathrm{mT}/\mu_0$.

To evaluate the magnetization dynamics, the free energy density is transformed to individual coordinate systems for the M_{A}- and M_{B}-sublattices, where the 3-axis is chosen along the equilibrium orientation of the respective sublattice magnetizations [38], while the 1- and 2-axes are along the dynamic components of $\boldsymbol{M}_{\mathrm{A,B}}$. We use an harmonic Ansatz ($M_{1,2} = m_{1,2}e^{i\omega t}$ and $M_3 = M_{\mathrm{A,B}}^{\mathrm{s}}$) to solve the linearized coupled Landau-Lifshitz equations

$$\begin{aligned} \frac{\partial\boldsymbol{M}_{\mathrm{A}}}{\partial t} &= -|\gamma_{\mathrm{A}}|\,\mu_0\boldsymbol{M}_{\mathrm{A}}\times\boldsymbol{H}_{\mathrm{eff,A}}, \\ \frac{\partial\boldsymbol{M}_{\mathrm{B}}}{\partial t} &= -|\gamma_{\mathrm{B}}|\,\mu_0\boldsymbol{M}_{\mathrm{B}}\times\boldsymbol{H}_{\mathrm{eff,B}}, \end{aligned} \tag{8}$$

where $\gamma_{\mathrm{A,B}}$ are the gyromagnetic ratios, assumed negative, of the respective sublattice magnetizations. The effective magnetic fields $\boldsymbol{H}_{\mathrm{eff,A}}$ and $\boldsymbol{H}_{\mathrm{eff,B}}$ are given by

$$\begin{aligned} \mu_0\boldsymbol{H}_{\mathrm{eff,A}} &= -\frac{\partial F}{\partial\boldsymbol{M}_{\mathrm{A}}}, \\ \mu_0\boldsymbol{H}_{\mathrm{eff,B}} &= -\frac{\partial F}{\partial\boldsymbol{M}_{\mathrm{B}}}. \end{aligned} \tag{9}$$

We formulate the eigenvalue problem in the form $\tilde{\chi}^{-1}\tilde{m}' = 0$, where $\tilde{m}'^{\intercal} = [m_{\mathrm{A},1}\; m_{\mathrm{A},2}\; m_{\mathrm{B},1}\; m_{\mathrm{B},2}]$ and the susceptibility $\tilde{\chi}$ is a 4×4 matrix. Resonance frequencies are obtained by setting $\det\tilde{\chi}^{-1} = 0$ and solving for ω. The parameters used for the simulation are summarized in the supplementary Table S1.